Stress Dependence of Optically Active Diamagnetic Point Defects in Silicon Oxynitride

Giuseppe Pezzotti,* Koichiro Hosokawa, Maria Chiara Munisso, Andrea Leto, and Wenliang Zhu

Ceramic Physics Laboratory and Research Institute for Nanoscience, Kyoto Institute of Technology, Sakyo-ku, Matsugasaki, 606-8585 Kyoto, Japan

Received: April 4, 2007; In Final Form: June 19, 2007

The cathodoluminescence (CL) spectrum arising from diamagnetic point defects of silicon oxynitride lattice was analyzed to extract quantitative information on local stress fields stored on the surface of a silicon nitride polycrystal. A calibration procedure was preliminarily made to obtain a relationship between CL spectral shift and applied stress, according to the piezo-spectroscopic effect. In this calibration procedure, we used the uniaxial stress field developed in a rectangular bar loaded in a four-point flexural jig. Stress dependence was clearly detected for the most intense spectral band of a doublet arising from diamagnetic (≡Si−Si≡) defects, which was located at around 340 nm. The shallow nature of the electron probe enabled the characterization of surface stress fields with sub-micrometer-order spatial resolution. As applications of the PS technique, the CL emission from ≡Si−Si≡ defects was used as a stress probe for visualizing the residual stress fields stored at grain-boundary regions and at the tip of a surface crack propagated in polycrystalline silicon nitride.

Introduction

The residual stress fields stored on the surface of ceramic materials (e.g., as arising from machining and polishing procedures) may play a significant role on the structural reliability of ceramic components and strongly affect the quality of deposited films when the ceramic part is used as a substrate. Besides making the material more or less prone to fracture, surface residual stress fields stored on a substrate surface may tangibly trigger extrinsic effects such as modulation of band gap and band structure in semiconductor films,[1] and preferential orientation of crystalline domains and textures in dielectric films.[2] In view of its importance in advanced technological applications, a precise evaluation of surface residual stresses is mandatory for both efficient design and reliability of advanced devices in many technological areas. In this context, the clarification and rationalization of the relationship between the crystallographic defect population existing in the material and the lattice strain stored nearby surfaces/interfaces is a keyfactor for miniaturized devices. A typical example is given by the requirement for very low leakage tunnel material in metal-oxide-semiconductor (MOS) structures, which may be strongly compromised by even a slight nonuniformity in both chemical composition and strain.[3]

Cathodoluminescence (CL) microscopy, although yet unexplored in its full potential as a spectroscopic tool, has been a standard technique for studying a great variety of materials over the past 20 years.[4,5] A limited number of early CL studies has been published for reference in solving metallurgical problems,[6,7] while great numbers of scanning electron microscopy−cathodoluminescence (SEM−CL) studies were published on semiconductor and phosphor ceramics.[8,9] The present authors have been recently applying CL microspectroscopy to the high spatially resolved assessment of residual and applied stress fields in a variety of ceramics, glasses, and semiconducting materials.[10−16] CL, which can be generally applied in conjunction with conventional SEM observation, may provide an immediate assessment with high spatial resolution of the distribution of surface stress fields. Identification is possible by CL, taking advantage of the piezo-spectroscopic (PS) effect, namely, the shift in wavelength of a luminescence transition in a stressed lattice as compared to a reference unstressed state.[17] CL microscopy utilizes an electron beam that interacts with the specimen surface. As a result of electron beam−specimen interaction, crystalline and amorphous phases in specimens produce characteristic CL spectral bands. Trace elements, lattice defects, or intrinsic properties within the crystal typically cause this emission of photons. Activators, such as transition metal ions (Mn^{2+}, Cr^{3+}, Fe^{3+}) and rare earth activators (Eu^{2+}, Sm^{3+}, Tb^{3+}, Dy^{3+}), can create strong luminescence if present even in trace amounts. Cation/anion vacancies and cluster defects can also cause CL. All these types of luminescence in principle obey the PS effect and can, if spectrally resolvable, be used as stress sensors in the material after performing appropriate PS calibrations.

In this paper, we attempt to explore the PS effect as it occurs in the CL emission from point defects in silicon nitride (Si_3N_4) and oxynitride (SiO_xN_y) surface structures. From a basic science point of view, this study is in line with and somehow completes our previous studies of PS effect in the optical emission of oxygen defects in oxide materials (e.g., the F^+-center luminescence of sapphire[10,11]). From a technological point of view, this work found its motivation in the need for developing a highly localized spectroscopic probe for silicon oxynitride electronic gates, due to recent trends in replacing the amorphous-gate silicon oxide adopted in MOS devices with oxynitride gates[18−21] or stacked oxide/nitride dielectrics.[22] We shall show here that, once CL spectra, PS procedures, and sample/probe interactions are fully rationalized and properly calibrated, defect luminescence may become a highly spatially resolved sensor for stress assessments in advanced electronic devices.

* Corresponding author. E-mail: pezzotti@kit.ac.jp.

10.1021/jp072667e CCC: $37.00
Published on Web 08/09/2007

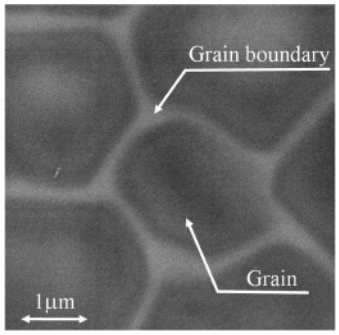

Figure 1. Typical FEG-SEM micrograph showing the microstructure of polycrystalline silicon nitride. Observation was made after thermal etching of a polished surface of the sample for 40 h at 1600 °C.

Materials and Methods

A fully dense polycrystalline Si_3N_4 sample was analyzed, which was obtained according to a hot-isostatic-press sintering cycle conducted at 2000 °C under 180 MPa isostatic Ar gas pressure. Prior to sintering, the sample was encapsulated into a Pyrex glass capsule to avoid infiltration of high-pressure Ar gas into the sample. No intentional addition of sintering aids or other external phases was made; however, an oxygen impurity was present in the material due to surface oxidation of the starting Si_3N_4 powder (E-10, UBE Industries, Ube, Japan). Such an impurity was present in the final sintered body mainly as a SiO_xN_y grain-boundary film, typically 1 nm in thickness, for a total fraction of about 2.4 vol % of the bulk material. The average grain size of the dense Si_3N_4 polycrystal was about 1.5 μm. Detailed explanations about material preparation and high-resolution microscopy observation of crystalline grains and grain-boundary structures have been given elsewhere.[23,24] The dense sample was polished with fine diamond paste (0.1 μm) in order to minimize the effect of residual stresses due to surface machining. The polished sample was eventually thermally etched (40 h at 1600 °C) in order to observe its microstructure and to compare it with the features revealed by luminescence maps collected on non-etched samples. A typical microstructural image of the etched surface of the investigated Si_3N_4 polycrystal is shown in Figure 1.

CL spectra were collected in a field-emission gun scanning electron microscope (FEG-SEM, SE-4300, Hitachi Co., Tokyo, Japan) equipped with a CL device. The CL device consisted of an ellipsoidal mirror and a bundle of optical fibers to collect and to transmit the CL emission into a spectrally resolved monochromator (Triax 320, Jobin-Yvon/Horiba Group, Tokyo, Japan). A 600 g/mm grating was used throughout the experiments. A liquid-nitrogen-cooled, 1024 × 256 pixels charge coupled device (CCD) was used to analyze the CL emission of the material.

The PS calibration method employed for generating a known stress field into the materials investigated was a four-point-bend loading microjig, which was equipped with a load cell of 100 N and placed into the electron microscope. By employing this jig, a bending bar made of the investigated material was loaded and luminescence spectra mapped along the sample thickness to calibrate the stress dependence of the selected CL band. A schematic draft of the bending calibration procedure, including the locations at which the CL signal was collected, is shown in Figure 2. A calibration procedure based on a four-point bending configuration involves both compressive and tensile uniaxial stresses, whose maxima in magnitude are found in correspondence with the centers of the loaded surfaces in contact with the short and the long span of the jig, respectively. As

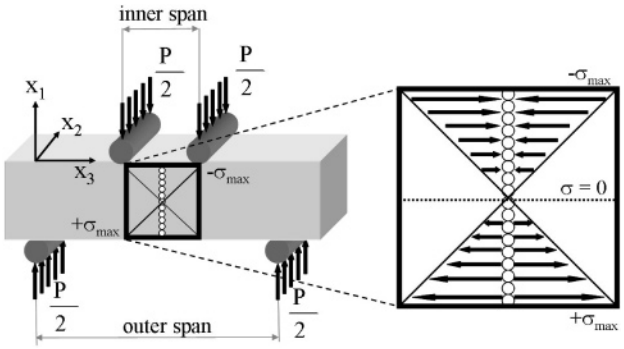

Figure 2. Schematic of the four-point-flexure setup used for the calibration procedure, including the locations at which the CL signal was collected in situ during loading of the sample. The selected system of Cartesian coordinates and a qualitative plot of the stress field developed along the thickness of the bending bar are also shown. In this latter plot the sign + and − to the maximum stress, σ_{max}, refer to a tensile and a compressive field, respectively.

long as the material response is kept in the elastic deformation region (i.e., as it has always been the case in the present study), the internal stress field can be considered to be linear along the thickness of the flexural bar and constant along its width.[25] During the time necessary for collecting in situ CL spectra for calibration, the externally applied load was continuously monitored and no significant relaxation in the loading jig could be detected.

Quantitative calibrations of the CL probe in the investigated material were carried out with using a bimaterial interface between the bulk Si_3N_4 sample and epoxy resin. Details of the probe calibration procedure have been given elsewhere.[11,13] The electron probe size was obtained from the experimental assessment of differential contributions from each volume portion of the luminescent probe. The intensity variation in the CL probe was retrieved from mathematical derivation of a plot of CL (relative) intensity as a function of distance between the bimaterial interface and the electron-irradiated probe center.[11,13]

Results and Discussion

A. CL Spectrum from Optically Active Defects. Rationalization of Si−Si bond formation in Si−O−N clusters can be obtained according to Mott's rule, which can be used to describe short-range order in silicon oxide, silicon nitride, and silicon oxynitride materials. Mott's rule can be expressed as follows:[26,27]

$$N_c = 8 - n \tag{1}$$

where N_c is the coordination number and n is the number of valence electrons. The Si atom has four valence electrons ($3s^2$-$3p^2$), and, according to eq 1, its $N_c = 4$. On the other hand, the O atom has six valence electrons ($2s^22p^4$). Therefore, in SiO_2 and *c*-Si_2N_2O, each O atom should be coordinated by two Si atoms. Similarly, the N atom possesses five valence electrons ($2s^22p^3$), and in Si_3N_4 and *c*-Si_2N_2O, each N atom is 3-fold-coordinated by Si atoms. Since an N atom in Si_3N_4 is coordinated by three Si atoms, and an O atom in SiO_2 is coordinated by two Si atoms, substitution of N by O should accompany the formation of a silicon dangling bond (or E′-center), ≡Si•, and to hole traps, ≡Si−Si≡, according to the two equilibrium equations:

$$2(\equiv Si_3N) + 2O \rightarrow 2(\equiv Si^{\bullet}) + 2(\equiv Si_2O) \tag{2}$$

$$\equiv Si^{\bullet} + {}^{\bullet}Si\equiv \rightarrow \equiv Si-Si\equiv \quad (3)$$

The silicon−silicon bond (≡Si−Si≡) has six external bonds that can be thus connected by O, N, and Si with different combinations. The creation of hole traps (Si−Si bonds) during oxidation of SiO_xN_y is related to the replacement of N atoms by O atoms.[28] More in general, the population of electronic defects generated by the trap in silicon nitride and oxynitride structures has been classified into (i) paramagnetic defects, such as ≡Si• (or P_b-center), ≡SiO•, and ≡Si_2N•; (ii) diamagnetic defect, such as ≡Si−Si≡; (iii) dicoordinated Si center, such as ═Si:; and (iv) hydrogen-related (or extrinsic) defects, such as ≡SiH, ≡Si_2NH, and ≡SiOH.

The P_b-center, which consists of a 3-fold-coordinated silicon atom with an unpaired electron, has been recognized as the major source of interface states at Si/SiO_2 interfaces.[29−31] However, silicon dangling bonds, ≡Si•, can be conspicuously removed by nitridation, and no CL emission is expected from those defects in silicon nitride and related compounds. On the other hand, the paramagnetic defect consisting of an oxygen atom with unpaired electron (≡SiO• or *R*-center, as commonly observed in amorphous silicon oxide) displays a clear red luminescence at around 1.9 eV.[32] The *R*-band can also be generated in the presence of ≡Si_2N• defects in nitride and oxynitride structures; however, the structure of the nitridated defect is significantly more complex than that in pure silica, because a random coordination can be obtained with different numbers of oxygen and nitrogen atoms; accordingly, band broadening and a slightly different peak energy (i.e., a shift toward lower energies) can be observed at relatively high nitrogen concentrations with respect to the conventional *R*-center.[33] On the other hand, the intensity of the *R*-center in oxynitride becomes higher as oxygen concentration (and, thus, the statistical presence of ≡SiO• with respect to ≡Si_2N• sites) increases.

The luminescence emission obtained from a diamagnetic trap, ≡Si−Si≡, consists of bands with energy at 3.16, 3.4−3.6, and 4.4−4.7 eV, which could be clearly observed in CL literature studies of nitride films.[28,33,34] The high-energy peak at 4.4 eV can be related to oxygen vacancies (i.e., the $O_3Si-SiO_3$ defect). A relatively strong doublet is reported in the interval 3.1−3.6 eV, as arising from the $N_3Si-SiN_3$ bond. Furthermore, the energy difference between σ-bonding and σ*-antibonding states of Si−Si bond in nitride is 4.6 eV, and it gives rise to an additional CL peak located at 4.7 eV, as a singlet−singlet transition in the $N_3Si-SiN_3$ bond.[34] The triplet−singlet transitions in the dicoordinated Si-center with two unpaired electrons, ═Si:, give rise to a blue band (at around 2.7 eV) in both silicon oxide and oxynitride structures, although the atomic configuration of this center may be different in the two structures. Hydrogen-related extrinsic defects have not so far been reported as being optically active in CL studies of nitride structures. A summary of the salient CL features reported for optically active defects in silica, silicon nitride, and oxynitride structures is given in Table 1.

Parts A and B of Figure 3 show typical CL emissions, collected in the spectral interval between the visible (blue) and the ultraviolet emission, from the Si_3N_4 grain interior and the SiO_xN_y grain-boundary region, respectively (cf. labels in the FEG-SEM micrograph of Figure 1). Spectra were deconvoluted into three Gaussian subbands, according to transitions related to diamagnetic and dicoordinated Si-center defects. Both spectra display an intense doublet arising from diamagnetic defects and related to the $N_3Si-SiN_3$ bond, in addition to the dicoordinated Si-center (═Si:) blue band located at around 2.7 eV. Interestingly, despite the significant difference in structure between bulk grains (mainly Si_3N_4) and grain-boundary channels (nitrogen-rich silicon oxynitride[35,36]), the relative intensities of the bands constituting the studied portion of the CL spectrum were found to be conspicuously constant. However, the absolute CL intensity was 4-fold higher at the grain interior as compared to grain boundaries. This latter feature can be easily explained by a more massive presence of $N_3Si-SiN_3$ bonds in the bulk grain structure. Additional features, explainable with consideration of the higher presence of oxygen bonds in the grain-boundary channels as compared to bulk grains, were observed in the red region (not shown here) of the CL spectrum (i.e., the *R*-band arising from the optical activity of paramagnetic defects). A full discussion of the CL spectrum of the material is beyond the scope of this paper and will be published elsewhere. Among the observed CL bands, of particular interest for our micromechanical studies is the stronger of two bands belonging to the ultraviolet diamagnetic doublet (with intensity maximum corresponding approximately to a wavelength of 340 nm). The observed invariance in relative intensity among spectra originated from different regions of the polycrystal helps to rule out any significant contribution from a local (relative) intensity change (i.e., statistical variations in defect population) to the observed band shift. The diamagnetic defect band will prove particularly useful in residual stress characterization because of its relatively sharp and intense nature and stress sensitivity.

TABLE 1: Cathodoluminescence Features of the Principal Defects Reported in Literature for Si_3N_4 and SiO_xN_y Materials[28,32−35]

defect type	energy (eV)	band maximum (nm)
$O_{3-\beta}N_\beta SiO$	1.9	652
O_2Si, N_2Si, or NOSi	2.7	459
$N_3Si-SiN_3$	3.1−3.6	400−344
≡Si−Si	4.4−4.7	281−263
≡$N_3Si-SiN_3$		
≡SiOO	5.4−5.7	229−217

B. PS Calibration of Diamagnetic Emission on Flexural Bar. The PS effect in a given electronic transition is represented by the wavelength shift, $\Delta\lambda$ (with respect to its unstressed state), to which the luminescence band representative of the transition undergoes in response to an applied or residual (elastic) stress field. In the general case, the stress state is represented by a second-rank tensor, σ_{ij}, which can be related to the scalar quantity, $\Delta\lambda$, according to a tensorial formalism first proposed by Grabner.[17] Although this formalism was originally proposed for luminescence arising from a chromophoric impurity embedded in a crystal lattice, we have recently extended its validity to the general case of point-defect luminescence, irrespective of the defect being a substitutional chromophoric atom or an optically active vacancy cluster.[10,11] The Grabner's tensorial equation is given as follows:

$$\Delta\lambda = \Pi_{ij}\sigma_{ij} = \Pi_{ii}\sigma^*_{ii} \quad (4)$$

where $i, j = 1, 2, 3$; $\Delta\lambda = \lambda - \lambda_0$ is the wavelength shift observed with respect to a reference "stress-free" wavelength, λ_0; the repetitive index notation is applied in eq 4; and Π_{ij} is referred to as the second-rank tensor of PS coefficients. An asterisk denotes the choice for the stress tensor of a set of Cartesian axes co-incident with the principal stress directions, eq 4 stating that the observed spectral shift is independent of the choice of Cartesian axes with the origin at the measurement location. In single-crystalline materials, the PS tensor always refers to the crystallographic axes of the crystal.[17] For the hexagonal structure of silicon nitride, crystallographic symmetry

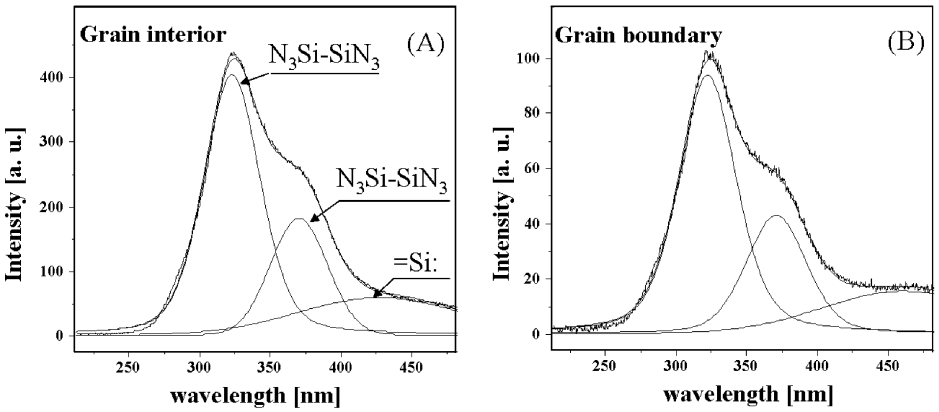

Figure 3. Typical CL spectra collected from the Si_3N_4 grain interior (A) and from the SiO_xN_y grain-boundary region (B). Spectral deconvolution into three Gaussian subbands is shown, according to transitions related to diamagnetic and dicoordinated Si-center defects.[28,32]

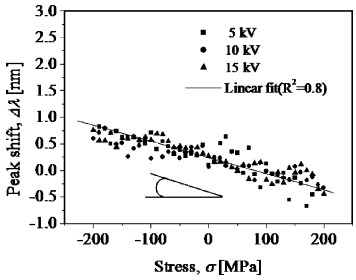

Figure 4. Results of uniaxial-bending PS calibration on the diamagnetic 340 nm band (after spectral deconvolution). Data obtained by scanning at different electron acceleration voltages are merged in the same plot, which was obtained by least-squares fitting to a linear function (correlation factor, $R^2 \cong 0.8$; slope, $\Pi = -2.50 \pm 0.03$ nm/GPa).

suggests that $\Pi_{11} = \Pi_{22} \neq \Pi_{33}$ (with the indexes 1, 2 referring to the crystallographic directions in the basal plane and index 3 referring to the *c*-axis of the crystal). In amorphous and nontextured polycrystalline material, provided that the PS measurement is averaged over a (statistically meaningful) large number of clusters or grains, the PS tensor reduces to an average scalar number, Π, which can be expressed as the average of the PS tensor components characteristic of the principal axes of the cluster or of the crystal:

$$\Pi = \frac{\Pi_{11} + \Pi_{22} + \Pi_{33}}{2} \tag{5}$$

In our PS bending calibration, the applied stress field was of a purely uniaxial type with $\sigma_{ij} = \sigma_{33} = \sigma$ (cf. Figure 2). In addition, each CL spectrum used for one data plot in the calibration was collected from a relatively large area ($\approx 50\ \mu_m^2$), thus representing the average of a relatively large number of grains and grain boundaries. Under these conditions, eq 4 simply reduces to a scalar equation, as follows:

$$\Delta\lambda = \Pi\sigma \tag{6}$$

The results of a uniaxial-bending PS calibration on the diamagnetic 340 nm band are shown in Figure 4. The scan across the loaded flexure bar was repeated with the electron beam set at different acceleration voltages. As can be seen, all the scans gave very close results and their cumulative plot could be indeed least-squares-fitted to a line with a good degree of approximation (correlation factor $R^2 \cong 0.8$). From the slope of the fitting line, an average PS coefficient could be obtained as $\Pi = -2.5 \pm 0.03$ nm/GPa. Besides spectroscopic errors, which in the present CL device only affected the Π value to its third decimal, the observed scatter (i.e., corresponding to an error on the stress assessment on the order of 15%) most likely arose from stress intensifications at grain boundaries and at small surface porosity and flaw locations. On the other hand, the reason why PS scans performed at different electron acceleration voltages gave very similar results resides in two factors: (i) the linear nature of the applied stress field makes it possible for an exact compensation between the parts of the broadened electron probe respectively reading higher and lower stress magnitudes with respect to the geometrical center of the electron beam (as theoretically and experimentally demonstrated in a previous paper)[12]; and, (ii) unlike microscopic PS calibration methods,[11,13,15,37] the size of the adopted electron probe was relatively small as compared with the stress gradient superimposed on the flexure bar (cf. probe size assessment in the next section), so that no probe deconvolution procedure was required for taking into account the finite size of the probe. It should be noted that, according to the spectral deconvolution procedure shown in section A, the present PS calibration used diamagnetic point defects as a sensor of stress in a Si_3N_4 lattice. Although nominally pure, the material was actually oxygen-contaminated and contained SiO_xN_y clusters due to oxidation of both the starting powder and free-surface structures. Although the PS coefficient obtained in this study was smaller (namely, the PS measurement was less sensitive) than that obtained by simply monitoring the shift of the cumulative diamagnetic-defect doublet band without any spectral deconvolution[37] (cf. cumulative band maximum in Figure 3), the present PS approach is more general because it does not include eventual band-shift contributions arising from local changes in defect population, and thus it should be considered more precise.

C. Size Calibration of the CL Probe. The size of the CL probe strongly depends on the acceleration voltage selected for electron impingement on the sample. When defect luminescence is probed,[10−12] a criterion of statistical consistency for the spectroscopic assessment may require that the probe volume contains at each probed location a statistically significant number of luminescent (defect) clusters. In addition, unlike some chromophoric and the totality of excitonic luminescence bands, the limited efficiency of the luminescence emitted from defects imposes the use of relatively large acceleration voltages in order to obtain a clear spectroscopic detection. Both these circumstances impose a lower limit for probe size and, thus, a critical value for the adopted acceleration voltage. On the other hand, in micromechanical assessments, the detected stress magnitude significantly scales down with increasing probe size, the observed stress magnitude being a weighted average over the entire probe volume. Therefore, a mandatory prerequisite in

order to avoid underestimation of the stress magnitude is to minimize probe size and intrusiveness. Given this important issue in PS assessments, detailed knowledge of probe morphology is required and this calls for a compromise between the obtained spatial resolution and the statistical reliability of the collected spectra.

The size of the CL probe depends on the nature of the interaction between solid target and electron beam. In the present silicon nitride material, we reliably obtained clear and stable spectra for acceleration voltages, $V \geq 3$ kV. To estimate the probe size, the *in-plane* probe response function (PRF) was experimentally retrieved from line scans across a sharp interface with a nonluminescent material. The PRF gives the distribution of luminescence emission inside the CL probe, which can be mathematically represented by a Gaussian equation:

$$G(x,x_0,V) = C_1 \exp\frac{-(x-x_0)^2}{C_2 V^n} \tag{7}$$

where the abscissas, x and x_0, represent a general point in the focal plane and the geometrical center of the focused electron beam, respectively, and the parameter C_1 can be taken equal to unity after normalization. In the first approximation, the luminescent probe can be taken to be symmetric in the measurement plane, and its size, R_{CL}, can be defined according to the following equation:

$$\frac{\int_{x_0-R_{CL}}^{x_0+R_{CL}} G(x,x_0,V)\,dx}{\int_{-\infty}^{+\infty} G(x,x_0,V)\,dx} = 0.9 \tag{8}$$

Note that the choice of the factor 0.9 in eq 8, although arbitrary, is based on the understanding that any contribution <10% to the CL intensity from remote parts of the electron probe will affect by a negligible amount the spectral shift of the band maximum, which we used to assess the stress magnitude. The CL probe size can be compared with the primary electron probe range, R_{el}, as a function of acceleration voltage, V. This latter parameter can be calculated according to the Kanaya−Okayama equation:[38]

$$2R_{el} = \frac{2.76 \times 10^{-2} A}{\rho Z^{0.889}} V^{1.67} \tag{9}$$

where ρ is the crystal density, A its atomic mass number, and Z its atomic number (e.g., 2.21 g/cm^3, 154 g/mol, and 20, respectively, for silicon nitride).

The results of CL intensity line scans as a function of electron acceleration voltages (for the interval 3 kV $\leq V \leq$ 9 kV) across a bimaterial interface are shown in Figure 5A. The differential contribution from each portion of volume in the luminescent probe, which is represented by the first derivative of the normalized intensity functions in Figure 5A, is shown in Figure 5B as a function of acceleration voltage. The best fit to the experimental data collected at different voltages was obtained, according to eq 7 and by selecting the probe-related parameters C_2 and n as 0.022 and 1.05, respectively. A plot of probe size as a function of acceleration voltage, $R_{CL}(V)$, was then obtained from the plots of Figure 5B, according to eq 8. This plot is given in Figure 6 and compared with a plot of electron probe size, as obtained according to eq 9. Note that, in the case of an electron probe, the in-plane probe size can be considered to be nearly the same as the probe depth in the investigated material.[39,40] Furthermore, as far as the order of magnitude of probe

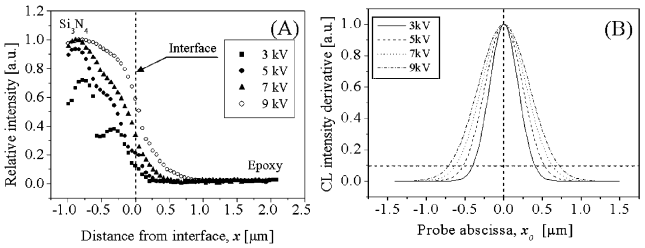

Figure 5. (A) CL relative intensity line scans at different electron acceleration voltages (in the interval 3 kV $\leq V \leq$ 9 kV) across an interface between polycrystalline silicon nitride and epoxy resin. (B) First derivative of the normalized plots (after least-squares fitting) in A, representing the electron probe response function of the polycrystal. The broken line represents the threshold value of 10% relative CL intensity selected for the definition of probe size in eq 8.

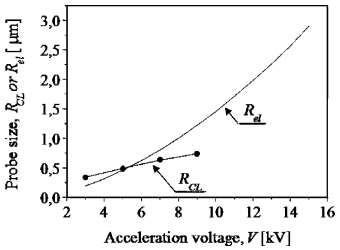

Figure 6. Plot of probe size as a function of electron acceleration voltage, $R_{CL}(V)$, as obtained from the experimental Gaussian plots in Figure 5B according to eq 8. A comparison is made with the primary electron probe range, $R_{el}(V)$, calculated according to eq 9.

size is concerned, the size of the electron probe is close to that of the luminescence probe. However, a closer look to probe-size plots reveals that at $V < 5$ kV, the R_{CL} is systematically larger than R_{el}, suggesting that internal optical diffusion contributes to the observed CL probe size as a consequence of the relatively high transparency of the silicon nitride material. On the other hand, for $V > 5$ kV, R_{CL} is lower than R_{el}, most likely due to internal absorption. Despite probe broadening, it is here demonstrated that the size of the CL probe can be confined into a sub-micrometer order, namely, a probe size (i.e., and in particular, a probe depth) significantly smaller than that achieved by conventional laser probes in silicon nitride materials.[40]

D. Applications and Technological Significance of PS Stress Assessment. We have shown in section B that, according to Grabner's formalism, we can obtain an estimate of the trace of the stress tensor at any location of the CL/PS assessment. In addition, stress fields measured with an extremely shallow CL probe can be simply considered with regard to their in-plane biaxial nature. However, error may be involved with just considering an average value for the PS coefficient (as described in section B); in fact, as far as a noncubic crystal is concerned, there is no precise knowledge about the crystallographic orientation of individual grains; the larger the anisotropy in the PS behavior of the crystal (e.g., the difference between the PS coefficients in the *a*- and *c*-planes of the crystal), the larger the error. This can be demonstrated by a comparison between the case of a general biaxial stress state, σ_{ii}^*, applied in the basal crystallographic (*c*-)plane of the hexagonal Si_3N_4 crystal as compared to the case of a biaxial stress state applied in the *a*-plane; eq 4 reduces to the two scalar eqs 10 and 11, respectively, as follows:

$$\Delta\lambda = \Pi_{11}\sigma_{11}^* + \Pi_{22}\sigma_{22}^* \equiv \Pi\sigma_{ii}^* \tag{10}$$

$$\Delta\lambda = \Pi_{22}\sigma_{22}{}^* + \Pi_{33}\sigma_{33}{}^* \equiv \Pi\sigma_{ii}^* \tag{11}$$

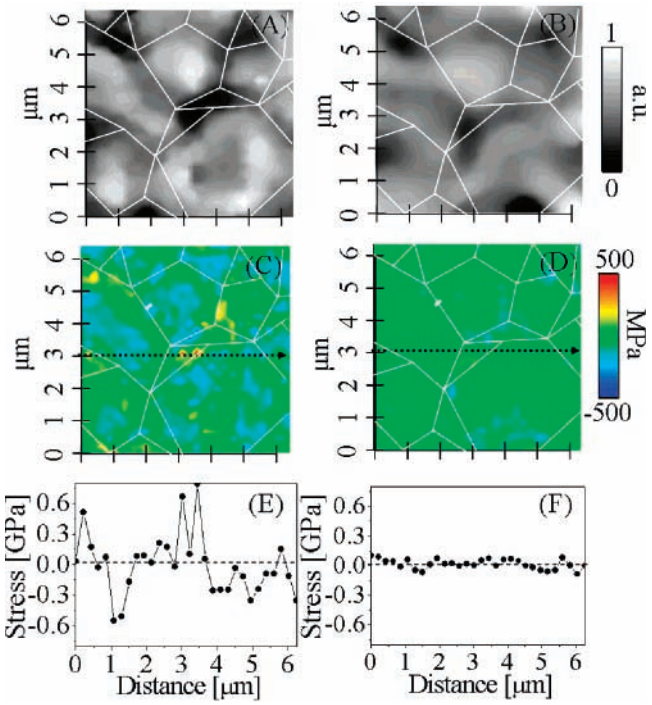

Figure 7. CL intensity maps of the cumulative UV spectrum of the investigated Si_3N_4 polycrystal collected at electron acceleration voltages of 3 (A) and 9 (B) kV. Residual stress maps obtained at the same location from the shift of the 340 nm CL band are shown in C and D for 3 and 9 kV, respectively. A linear profile of trace stress magnitude, from an arbitrarily selected horizontal line in the map (the selected line corresponds to the broken line indicated in both C and D) are shown in E and F.

where, in eq 10, $\Pi = \Pi_{11} = \Pi_{22}$ and $\sigma^*_{ii} = \sigma^*_{11} + \sigma^*_{22}$ is the trace of the principal stress tensor, while, in eq 11, $\Pi = (\Pi_{22} + \Pi_{33})/2$ (with $\Pi_{22} \neq \Pi_{33}$) and $\sigma^*_{ii} = \sigma^*_{22} + \sigma^*_{33}$. Two main difficulties hampered a more precise evaluation of the PS tensor in order to clear up this systematic error: (i) the fact that, unlike sapphire,[10,11] neither a Si_3N_4 nor a SiO_xN_y single crystal of sufficiently large dimensions was at this time available for our CL/PS calibrations; and (ii) the crystallographic orientation of individual grains in the polycrystalline texture revealed on the polished plane could not be evaluated. It should be noted that the approximations involved in our PS measurements of a polycrystalline material should disappear in technologically interesting MOS applications (i.e., mainly dealing with amorphous SiO_xN_y structures). Albeit approximated, we attempt hereafter the visualization of residual stress states stored on a sub-micrometer scale in the polycrystalline Si_3N_4 structure using the diamagnetic defect band located at 340 nm as a stress sensor.

Parts A and B of Figure 7 show CL intensity maps of the cumulative UV spectrum of the investigated Si_3N_4 polycrystal collected at two different acceleration voltages (3 and 9 kV, respectively). The spatial resolution (i.e., the CL probe radius/depth) of these two maps corresponded to about 300 and 700 nm, respectively, according to the experimental plot in Figure 6. As seen, the two maps, collected from the same area, reveal grain-boundary features in their darker zones (cf. Figure 1), which were not visible in the conventional FEG-SEM observation of the polycrystalline surface in its non-etched state. The lack of CL intensity at grain boundaries can be explained according to the explanation given in section A about the statistical relevance of diamagnetic sites in the defect population of bulk Si_3N_4 as compared to the grain-boundary SiO_xN_y structure. Parts C and D of Figure 7 show the residual stress maps obtained at the same location by a PS approach on the 340 nm CL band (i.e., after spectral deconvolution according to Figure 3A,B). Two main features were revealed in these two latter maps: (i) the stress state tends to be compressive inside the Si_3N_4 grains and tensile at grain boundaries, with significant tensile stress intensification at multiple grain junctions; and (ii) the internal stress distribution is clearly smoothed down by enlarging the probe size (i.e., by increasing to 9 kV the adopted acceleration voltage of the electron beam); in particular, the trace stress magnitude at grain boundaries was largely reduced and no significant stress intensification could be detected. To make it clearer the difference in the detected stress magnitude obtained at different electron acceleration voltages, we have plotted below each map (Figure 7E,F) a linear profile of trace stress magnitude, from an arbitrarily selected horizontal line in the map (the selected line corresponds to the broken line indicated in both C and D of Figure 7). This typical example of micromechanical CL/PS characterization clearly emphasizes the importance of adopting a sharp electron probe in assessing highly graded and localized stress fields.

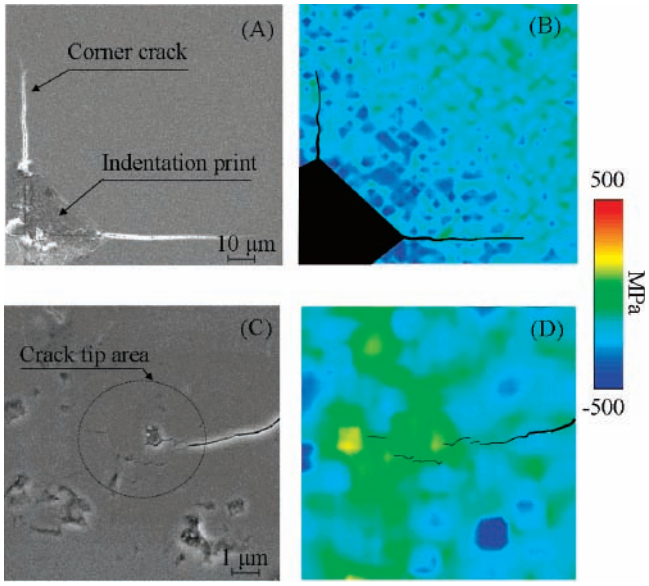

Figure 8. FEG-SEM micrograph of an indentation printed on the Si_3N_4 surface (A) and its related residual stress map (B), as obtained by using diamagnetic defects as stress sensor. Panels C and D show a high-resolution FEG-SEM view of the tip of a crack propagated from an indentation corner and its related residual stress map, respectively.

An additional example of a highly localized/graded stress field is represented by the residual stress field stored in the neighborhood of an indentation print and, in particular, the stress intensification piled up in front of the tip of the microcracks propagated from the corners of the print. Parts A and B of Figure 8 show a FEG-SEM micrograph of an indentation printed on the surface of the investigated polycrystalline Si_3N_4 and its related residual stress map collected using diamagnetic defects as stress-sensitive clusters, respectively. In PS assessments, the sample was impinged with an electron beam of acceleration voltage of 3 kV and probe current of 120 pA. The indentation print was found embedded into a compressive residual stress field of magnitude up to 500 MPa. Such a stress field extended farther away from the indentation center to remote zones ahead of the tip of corner cracks. Parts C and D of Figure 8 represent a high-resolution FEG-SEM view of the tip of a corner crack and its related residual stress map, respectively. The overall residual stress field is clearly given by the overlap of the compressive stress field associated with the indentation print (i.e., in which the crack is embedded) and the tensile stress field

associated with the presence of the equilibrium crack. Although the compressive stress field may somewhat reduce the crack-tip stress field, a clear intensification of stress, tensile in nature, could be observed along a bifurcated line ahead of the crack tip, which most likely lies in correspondence of grain boundaries to be fractured in further crack propagation.

The continuing progress in miniaturizing electronic devices and controlling their defect population and interface structures represents a great challenge from the viewpoint of microscopic stress characterization. We have shown the feasibility of assessing stress patterns on a sub-micrometer scale in silicon nitride and related materials, and there is an ongoing challenge on pushing the stress measurement toward the single-nanometer scale through improving the CL detection efficiency at low acceleration voltages. With CL having the advantage of easy compatibility with real-time surface screening by scanning electron microscopy, areas of devices with a faulted structure or highly stressed (i.e., more prone to fracture) can be promptly individuated in a nondestructive manner.

Conclusion

Spectrally resolved CL spectroscopy coupled with a highly focused low-energy electron beam allowed localized stress assessments in Si_3N_4 and SiO_xN_y materials. Trace stress tensor assessments could be obtained through the PS effect (i.e., by monitoring the wavelength shift) of the stronger band of a CL doublet arising from diamagnetic point defects. A standard (uniaxial) PS calibration procedure in bending has been applied to extract the stress information within a degree of accuracy. The size of the CL probe was also quantitatively assessed by experimentally evaluating the electron probe response function of the material. In this context, a clear improvement in spatial resolution as compared to a more conventional photostimulated PS approach could be found. Two applications of the technique have also been shown, by which we visualized microscopic surface stress fields ahead of the tip of a propagating crack and the residual stress intensification at the grain boundaries of a polycrystalline structure. Despite the approximations involved with the application of the CL/PS technique to a noncubic crystalline structure, the given examples vividly illustrate the experimental feasibility of high-resolution CL stress analysis and their possible application to oxynitride-based electronics devices.

References and Notes

(1) Miwa, K.; Fukumoto, A. *Phys. Rev. B* **1993**, *48*, 7897.
(2) Hubert, C.; Levy, J.; Carter, A. C.; Chang, W.; Kiechoefer, S. W.; Horwitz, J. S.; Chrisey, D. B. *Appl. Phys. Lett.* **1997**, *71*, 3353.
(3) Degraeve, R.; Kaczer, B.; Groeseneken, G. *Microelectron. Reliab.* **2000**, *40*, 697.
(4) Marshall, D. J. *Cathodoluminescence of Geological Materials*; Unwin Hyman: London, 1988; pp 1−93.
(5) Götze, J.; Plötze, M.; Habermann, D. *Mineral. Petrol.* **2001**, *71*, 225.
(6) Balyts'kyi, O. I. *Mater. Sci.* **1998**, *34*, 279.
(7) Hagni, R. D. Industrial Application of Cathodoluminescence Microscopy. *Process Mineralogy VI*; TMS-AIME: Warrendale, PA, 1986; pp 37−54.
(8) Yacobi, B. G.; Holt, D. B. *J. Appl. Phys.* **1986**, *59*, R1.
(9) Richards, B. P.; Trigg, A. D.; King, W. G. *Scanning* **1984**, *6*, 8.
(10) Pezzotti, G.; Wan, K.; Munisso, M. C.; Zhu, W. *Appl. Phys. Lett.* **2006**, *89*, 041908.
(11) Munisso, M. C.; Zhu, W.; Leto, A.; Pezzotti, G. *J. Phys. Chem. A* **2007**, *111*, 3526.
(12) Pezzottim, G.; Zhu, W.; Leto, A.; Matsutani, A.; Porporati, A. A. *J. Phys D.* **2006**, *39*, 4975.
(13) Porporati, A. A.; Tanaka, Y.; Matsutani, A.; Zhu, W.; Pezzotti, G. *J. Appl. Phys.* **2006**, *100*, 083515.
(14) Wan, K.; Porporati, A. A.; Feng, G.; Yang, H.; Pezzotti, G. *Appl. Phys. Lett.* **2006**, *88*, 251910.
(15) Porporati, A. A.; Hosokawa, K.; Zhu, W.; Pezzotti, G. *J. Appl. Phys.* **2006**, *100*, 093508.
(16) Zhu, W.; Porporati, A. A.; Matsutani, A.; Lama, N.; Pezzotti, G. *J. Appl. Phys.* **2007**, *101*, 103531.
(17) Grabner, L. *J. Appl. Phys.* **1978**, *49*, 580.
(18) Gritsenko, V. A.; Svitasheva, S. N.; Petrenko, I. P.; Wong, H.; Xu, J. B.; Wilson, I. H. *J. Electrochem. Soc.* **1999**, *146*, 780.
(19) Gritsenko, V. A.; Petrenko, I. P.; Svitasheva, S. N.; Wong, H. *Appl. Phys. Lett.* **1998**, *72*, 462.
(20) Wong, H.; Yang, B. L.; Cheng, Y. C. *Appl. Surf. Sci.* **1993**, *72*, 49.
(21) Wong, H.; Cheng, Y. C. *J. Appl. Phys.* **1990**, *67*, 7132.
(22) Morokov, Y. N.; Novikov, Y. N.; Gritsenko, V. A.; Wong, H. *Microelectron. Eng.* **1999**, *48*, 175.
(23) Tanaka, I.; Pezzotti, G.; Okamoto, T.; Miyamoto, Y.; Koizumi, M. *J. Am. Ceram. Soc.* **1989**, *72*, 1656.
(24) Pezzotti, G.; Ota, K.; Kleebe, H.-J. *J. Am. Ceram. Soc.* **1996**, *79*, 2237.
(25) Evans, A. G. *Progr. Mater. Sci.* **1976**, *21*, 171.
(26) Gritsenko, V. A.; Xu, J. B.; Kwok, R. W. M.; Ng, Y. H.; Wilson, I. H. *Phys. Rev. Lett.* **1998**, *81*, 1054.
(27) Street, R. A. *Phys. Rev. Lett.* **1982**, *49*, 1187.
(28) Gritsenko, V. A.; Shavalgin, Yu. G.; Pundur, P. A.; Wong, H.; Kwok, W. M. *Philos. Mag. B* **2000**, *80*, 1857.
(29) Matsuoka, T.; Taguchi, S.; Ohtsuka, H.; Taniguchi, K.; Hamaguchi, C.; Kakimoto, S.; Uda, K. *IEEE Trans. Electron Devices* **1996**, *43*, 1364.
(30) Lenahan, P. M.; Dressendorfer, P. V. *J. Appl. Phys.* **1984**, *55*, 3495.
(31) Edvards, A. H.; Pickard, J. A.; Stahlbish, R. E. *J. Non-Cryst. Solids* **1994**, *179*, 148.
(32) Leto, A.; Porporati, A. A.; Zhu, W.; Green, M.; Pezzotti, G. *J. Appl. Phys.* **2007**, *101*, 438.
(33) Wong, H.; Gritsenko, V. A. *Microelectron. Reliab.* **2002**, *42*, 597.
(34) Pundur, P. A.; Shavalgin, J. G.; Gritsenko, V. A. *Phys. Status Solidi A* **1986**, *94*, K107.
(35) Pan, X.; Gu, H.; van Weeren, R.; Danforth, S. C.; Cannon, R. M.; Rühle, M. *J. Am. Ceram. Soc.* **1996**, *79*, 2313.
(36) Kleebe, H.-J. *J. Ceram. Soc. Jpn* **1997**, *105*, 453.
(37) Pezzotti, G. *Key Eng. Mater.* **2005**, *287*, 438.
(38) Kanaya, K.; Okayama, S. *J. Phys. D* **1972**, *5*, 43.
(39) Donolato, C. *Phys. Rev. B* **1996**, *54*, 1478.
(40) Pezzotti, G. *J. Raman Spectrosc.* **1999**, *30*, 867.